



# Phase evolution of radio frequency magnetron sputtered Cr-rich $(\text{Cr,Zr})_2\text{O}_3$ coatings studied by in situ synchrotron X-ray diffraction during annealing in air or vacuum

Ludvig Landälv<sup>1,5,a)</sup> , Lina Rogström<sup>2</sup>, Jun Lu<sup>1</sup>, Daniel Ostach<sup>3</sup>, Fredrik Eriksson<sup>1</sup>, Muhammad Junaid<sup>1</sup>, Naureen Ghafoor<sup>1</sup>, Erik Ekström<sup>1</sup>, Ching-Lien Hsiao<sup>1</sup>, Harald Leiste<sup>4</sup>, Mats Ahlgren<sup>5</sup>, Emmanuelle Göthelid<sup>5</sup>, Björn Alling<sup>6</sup>, Lars Hultman<sup>1</sup>, Michael Stüber<sup>4</sup>, Norbert Schell<sup>3</sup>, Jens Birch<sup>1</sup>, Per Eklund<sup>1,b)</sup> 

<sup>1</sup>Thin Film Physics Division, Department of Physics, Chemistry, and Biology (IFM), Linköping University, Linköping SE-581 83, Sweden

<sup>2</sup>Nanostructured Materials, Department of Physics, Chemistry and Biology (IFM), Linköping University, Linköping SE 581 83, Sweden

<sup>3</sup>Institute of Materials Research, Helmholtz-Zentrum Geesthacht, Max-Planck-Str. 1, D-215 02 Geesthacht, Germany

<sup>4</sup>Karlsruhe Institute of Technology (KIT), Institute for Applied Materials (IAM), Eggenstein-Leopoldshafen 763 44, Germany

<sup>5</sup>Sandvik Coromant AB, Stockholm SE-126 80, Sweden

<sup>6</sup>Theoretical Physics, Department of Physics, Chemistry, and Biology (IFM), Linköping University, Linköping SE-581 83, Sweden

<sup>a)</sup>Address all correspondence to these authors. e-mail: ludvig.landalv@liu.se

<sup>b)</sup>e-mail: per.eklund@liu.se

Received: 23 April 2019; accepted: 17 October 2019

The phase evolution of reactive radio frequency (RF) magnetron sputtered  $\text{Cr}_{0.28}\text{Zr}_{0.10}\text{O}_{0.61}$  coatings has been studied by in situ synchrotron X-ray diffraction during annealing under air atmosphere and vacuum. The annealing in vacuum shows t-ZrO<sub>2</sub> formation starting at ~750–800 °C, followed by decomposition of the  $\alpha$ -Cr<sub>2</sub>O<sub>3</sub> structure in conjunction with bcc-Cr formation, starting at ~950 °C. The resulting coating after annealing to 1140 °C is a mixture of t-ZrO<sub>2</sub>, m-ZrO<sub>2</sub>, and bcc-Cr. The air-annealed sample shows t-ZrO<sub>2</sub> formation starting at ~750 °C. The resulting coating after annealing to 975 °C is a mixture of t-ZrO<sub>2</sub> and  $\alpha$ -Cr<sub>2</sub>O<sub>3</sub> (with dissolved Zr). The microstructure coarsened slightly during annealing, but the mechanical properties are maintained, with no detectable bcc-Cr formation. A larger t-ZrO<sub>2</sub> fraction compared with  $\alpha$ -Cr<sub>2</sub>O<sub>3</sub> is observed in the vacuum-annealed coating compared with the air-annealed coating at 975 °C. The results indicate that the studied pseudo-binary oxide is more stable in air atmosphere than in vacuum.

## Introduction

Oxide ceramics such as alumina, chromia, and zirconia are important materials for cutting tool development mainly due to their high hot hardness, chemical inertness with respect to work piece material, and oxidation resistance [1]. Thin (1–20 μm) coatings of these materials on a less brittle tool body benefit from otherwise counteracting material properties, yielding highly wear-resistant tools. Using physical vapor deposition (PVD) techniques to deposit these coatings permits lower substrate temperatures than the traditionally used chemical vapor deposition (CVD) and possible residual stress tailoring. PVD therefore allows deposition on temperature-sensitive substrates such as high-speed steels, opening up application areas for oxide coatings not readily accessible by CVD.

An important focus in the context of PVD-coated oxides for cutting tools has been the Al–Cr–O system. The goal has been to stabilize the corundum phase,  $\alpha$ -Al<sub>2</sub>O<sub>3</sub>, at lower deposition temperatures than in CVD with the help of isostructural  $\alpha$ -Cr<sub>2</sub>O<sub>3</sub> [2, 3]. Eskolaite ( $\alpha$ -Cr<sub>2</sub>O<sub>3</sub>) is one of the hardest naturally occurring oxides, ~30 GPa (measured with nanoindentation), and has been obtained by sputter deposition [4, 5]. Stabilization of the  $\alpha$ -Al<sub>2</sub>O<sub>3</sub> can be done by template growth on, e.g.,  $\alpha$ -Cr<sub>2</sub>O<sub>3</sub> [4, 6, 7] or by solid solution alloying of, e.g.,  $\alpha$ -(Al,Cr)<sub>2</sub>O<sub>3</sub> [3, 8, 9, 10, 11, 12, 13, 14]. Another possible phase on  $\alpha$ -Al<sub>2</sub>O<sub>3</sub> alloying with Cr is the cubic B1-like vacancy-stabilized structured (Al,Cr)<sub>2</sub>O<sub>3</sub> [2, 15, 16].

ZrO<sub>2</sub> exists in several thermodynamically stable crystal structures in its pure form: the room temperature (RT) monoclinic

(m) phase, tetragonal from  $\sim 1170$  °C, and cubic fluorite from  $\sim 2300$  °C [17, 18, 19]. The high-temperature phases are metastable at RT but can become stable through alloying at RT. The tetragonal phase (t) is stabilized by alloying with early transition metal oxides, often  $Y_2O_3$  [20, 21]. Tetragonal yttria partially stabilized zirconia (YSZ), containing 6–8 wt% of  $Y_2O_3$ , is often used as the principal material for thermal barrier coatings in turbines due to its low thermal conductivity and high toughness [22, 23, 24, 25]. YSZ also often finds its use as implant material owing to its biocompatibility [26]. Grain refinement, if below  $\sim 30$  nm, is another way of stabilizing tetragonal (t)- $ZrO_2$  even in pure form due to its lower surface energy compared with the monoclinic phase [27, 28]. For its ionic conductance, the cubic fluoride (stabilized with  $>8$  wt%  $Y_2O_3$ ) form is used as electrolyte in solid oxide fuel cells [29, 30, 31, 32, 33] and as material with reversible oxygen storage capacity when alloyed with  $CeO_2$  [34, 35].

These common materials are the basis for the motivation for the choice of the Cr–Zr–O system studied here. Replacing Al in the pseudo-binary alloy Al–Cr–O system with Zr yields another material system that may combine the interesting properties of the respective pure oxides. Previous work on the Cr–Zr–O system encompasses bulk mixing [36], nanoparticles [37, 38], and composite material of  $Cr_2O_3$  and YSZ [39].  $\alpha$ -(Cr,Zr) $_2O_3$  solid solution (Zr < 8.5 at%) thin film by reactive radio frequency (RF) magnetron sputtering was also reported [40], even though Zr is preferably in a  $Zr^{4+}$  (0.72 Å) state and larger than  $Al^{3+}$  (0.535 Å) [41].

Rafaja et al. [42] deposited amorphous Cr-rich Cr–Zr–O thin films with up to 15 at.% Zr content and performed in situ synchrotron-based X-ray diffraction (XRD) while vacuum annealing (500–1100 °C). The Zr content in the high-temperature crystallized  $\alpha$ -(Cr,Zr) $_2O_3$  contained up to 3.2 at.% Zr, while the excess Zr formed tetragonal  $ZrO_2$ , stabilized by Cr. Coatings deposited with higher Zr content resulted in higher temperature for onset of crystallization and degree of t- $ZrO_2$  phase formation.

In contrast to the as-grown amorphous coatings in this material system,  $\alpha$ -phase (Cr,Zr) $_2O_3$  solid solution coatings were grown at 500 °C by Spitz et al. [40]. The thermal stability and microstructural changes of this pseudo-binary oxide system were investigated by vacuum annealing at three different temperatures, 750, 810, and 870 °C, in our previous work [43]. The study showed a slight increase in hardness on formation of t- $ZrO_2$  with dissolved Cr after annealing to 810 °C, but the coating decomposed into t- $ZrO_2$  and bcc-Cr on loss of oxygen after annealing to 890 °C. The effect of annealing atmosphere on the coating thermal stability remained unexplored and merits further study.

Therefore, the aim of the present study was to determine the thermal stability and phase evolution of the Cr-rich,

$Cr_{0.28}Zr_{0.10}O_{0.61}$ , coating from earlier work [43] both in vacuum and in air atmosphere and at higher maximum annealing temperature. The phase evolution during annealing was monitored continuously through in situ XRD at the synchrotron facility, DESY in Hamburg. Using the synchrotron radiation setups, the change in coating crystal structure could be monitored continuously up to a maximum temperature of  $\sim 1140$  °C in vacuum and at 975 °C in air. Post-annealing characterization with transmission electron microscope (TEM) and scanning electron microscope (SEM) and nanoindentation hardness measurements corroborated the findings from high temperature XRD, mainly, that better thermal stability was obtained if annealed in air than in vacuum.

## Results

### Chemical composition and hardness

Table I shows the chemical composition of the coatings in the as-deposited state and after annealing. The chemical composition of the as-deposited coating was measured in the previous study with electron probe microanalysis (EPMA) [43] and remeasured in the present work with the top-view energy-dispersive X-ray spectroscopy (EDX). Both methods show that the as-deposited coatings is Cr-rich (Cr,Zr) $_2O_3$ , close to stoichiometric composition with respect to oxygen. The close compositional agreement between EPMA and EDX strengthens the validity of the EDX analysis of the as-annealed compositions. The results show that the coating annealed in air to 975 °C has the same composition as the as-deposited coating. However, for the coating annealed in vacuum, with 50 °C/min to a maximum temperature of 1140 °C, the Cr/Zr ratio reduced to 0.48 compared with  $\sim 2.9$  in the as-deposited state. Also, about 5 at.% reduced oxygen is measured after vacuum annealing, and for 2 at.% Ti, see the discussion for further explanation.

**TABLE I:** Chemical composition measured with EDX and nanoindentation hardness of the as-deposited and annealed Cr–Zr–O coatings. The compositional balance consist of C and N and traces of Ar based on reference EPMA measurement from Ref. 43. The standard deviations are  $\sim 0.5$  at.% or below for Cr, Zr, and O. C has been omitted for the EDX measurements due to lower than 1 at.% content when measured with EPMA.

Coating variants	Elemental composition (at.%)						Hardness (GPa)
	Cr	Zr	O	Ti	$\frac{Cr}{Zr}$	$\frac{Cr+Zr}{O}$	
As-deposited (500 °C) with EDX	29	10	61	...	2.9	0.64	$19.6 \pm 1.9$
Annealed in air to 975 °C with EDX	29	11	60	...	2.6	0.67	$22.3 \pm 2.3$
Annealed in vacuum to 1140 °C with EDX	14	29	55	2	0.48	0.78	$8.5 \pm 1.1$

The measured nanoindentation hardness, presented in the last column in Table I, yields a value of  $19.6 \pm 1.9$  GPa for the as-deposited coating. The air-annealed sample shows slightly increased average hardness  $22.3 \pm 2.3$  GPa; however, a larger number of invalid curves are observed. In contrast to the air-annealed sample, the vacuum-annealed coating shows a significant drop in hardness to  $8.5 \pm 1.1$  GPa.

### TEM and in situ XRD of vacuum-annealed sample

Figure 1 shows in situ X-ray diffractograms acquired during vacuum annealing with a heating rate of  $50\text{ }^\circ\text{C}/\text{min}$ . The most prominent coatings peaks, without substrate overlaps, appeared within  $d$ -spacing range of  $2.5\text{--}4\text{ \AA}$  and therefore chosen here from the total acquired  $1\text{--}5.5\text{ \AA}$  range. The short double dotted line, at a  $d$ -spacing of  $2.7\text{ \AA}$ , shows the RT position of the  $\alpha$ -(104)-(Cr,Zr) $_2\text{O}_3$  solid solution peak, as determined in previous work [43]. Here, it is shifted to a slightly larger  $d$ -spacing due to thermal expansion of the coating at  $500\text{ }^\circ\text{C}$ .

The two  $\alpha$ -Cr $_2\text{O}_3$  peaks visible in this range, namely, (104) and (012), are significantly shifted to larger  $d$ -spacing compared with reference  $\alpha$ -Cr $_2\text{O}_3$  (PDF-38-1479) marked with solid black lines. As found in previous work [43], this larger shift is due to the incorporation of Zr in the  $\alpha$ -Cr $_2\text{O}_3$  structure. With increasing annealing temperature, the  $\alpha$ -Cr $_2\text{O}_3$  peaks

remain at their respective  $d$ -spacing up to  $\sim 900\text{ }^\circ\text{C}$ , with an increase in the peak/background intensity. At temperatures higher than  $\sim 975\text{ }^\circ\text{C}$ , the peak intensity decreases at the same time as the peaks shift to smaller  $d$ -spacing's, prominent for the (104) peak. At around  $800\text{ }^\circ\text{C}$ , a new peak appeared at  $2.97\text{ \AA}$ , matching the (101) tetragonal-(t)-ZrO $_2$  (PDF-42-1164), but at slightly smaller  $d$ -spacing. Note that the diffraction pattern in PDF-42-1164 was acquired at  $1250\text{ }^\circ\text{C}$ , which helps explaining the gradual shift toward the high temperature measured  $d$ -spacing. Its intensity increases rapidly from  $\sim 945\text{ }^\circ\text{C}$  to  $\sim 1000\text{ }^\circ\text{C}$ , where it starts to decrease. The decrease in intensity is possibly due to the movement of the sample out of the beam (seen by increased intensity for the initially low intensity substrate peaks, i.e., at  $3.45\text{ \AA}$ ). Two additional t-ZrO $_2$  diffraction peaks, around  $2.6\text{ \AA}$ , are also observed at temperatures higher than  $1000\text{ }^\circ\text{C}$ . At smaller lattice spacing, Figs. S2–S4, bcc-Cr peaks (PDF-6-694) can be observed at  $2.06\text{ \AA}$  (110),  $1.19\text{ \AA}$  (211), and  $1.03\text{ \AA}$  (220), all shifted  $\sim 1.3\%$  to larger lattice spacing compared with the PDF values at RT. The most prominent and nonoverlapping peak at elevated temperatures is the (211), which shows a drastic peak intensity increase, Fig. S2, in the same temperature range as the t-ZrO $_2$  max intensity. This observation also correlates with the decrease in the  $\alpha$ -(Cr,Zr) $_2\text{O}_3$  phase around  $950\text{--}1050\text{ }^\circ\text{C}$ , see Fig. 1. The metallic Cr adhesion layer is the origin to the RT bcc-Cr peak

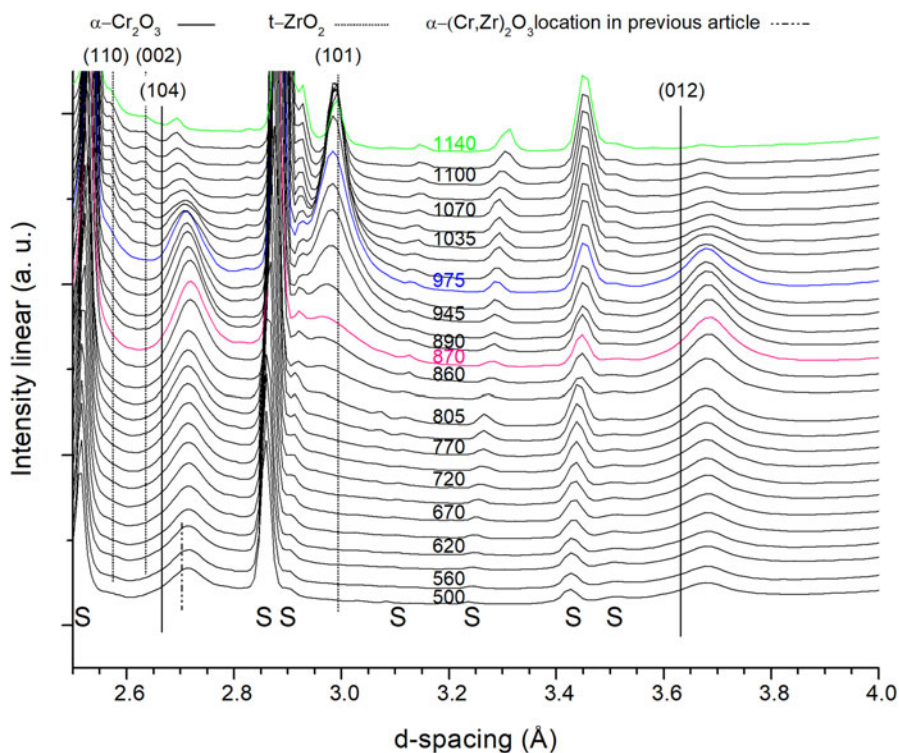


**Figure 1:** X-ray diffractograms of the coating annealed in vacuum up to  $1140\text{ }^\circ\text{C}$ . S = substrate. Green = maximum annealing temperature in vacuum, blue = maximum temperature achieved when annealing in air, and magenta = isothermal vacuum annealing temperature from previous work. Curves shifted for clarity. Temperature is given in  $^\circ\text{C}$ .

before annealing, situated at slightly lower  $d$ -spacing than after annealing, Fig. S3.

Figure 2 shows synchrotron XRD pattern before (red) and after (gray) vacuum annealing and the substrate before annealing (black). The peaks visible after annealing at 2.96 Å (101), 2.63 Å (002), and 2.55 Å (110) are attributed to the respective  $t$ -ZrO<sub>2</sub> planes, shifted to smaller  $d$ -spacing compared to the PDF-card high temperature values. The peaks at 3.69 Å (110), 3.63 Å (011), and 3.16 Å (−111) are attributed to the monoclinic ZrO<sub>2</sub> phase (PDF-37-1484). No peaks related to the  $\alpha$ -Cr<sub>2</sub>O<sub>3</sub> phase are observed.

Figure 3(a) shows the scanning transmission electron microscope (STEM) EDX map of a sample after vacuum annealing to 1140 °C. The red areas are Cr-rich and the turquoise areas are Zr-rich. Selected area electron diffraction (SAED) patterns (not shown) from two grains along different zone axis,  $\langle 111 \rangle$  and  $\langle 1\bar{1}0 \rangle$ , being rich in Cr in the EDX map, confirms bcc-Cr in these regions. The readers are directed to Ref. 43 for details on the bcc-Cr identification [43]. Figure 3(b) shows a higher magnification map of the area marked with a white box in (a). This magnification matches the map in Fig. 3(c), which shows an STEM EDX map of an isothermally vacuum-annealed sample at 870 °C from Ref. 43. It is clear that both the Cr- and Zr-rich grains are significantly larger in the present study, especially the Zr-rich phase. The ZrO<sub>2</sub> phase identification is based on the synchrotron XRD data in

combination with TEM-EDX mapping showing Zr-rich regions. Another mapping (not shown), including the substrate-coating interface, shows continuous layers of the binding layers, with segregated Cr and Zr, still present after the high-temperature annealing.

### TEM and in situ XRD of air-annealed sample

Figure 4 shows a fraction of in situ X-ray diffractograms from the sample annealed in air. The increase in the background for larger  $d$ -spacing originates from more air scattering at lower angles. This was reduced in the vacuum setup by the experimental setup.

The two  $\alpha$ -Cr<sub>2</sub>O<sub>3</sub> peaks visible in this range, (104) and (012), are significantly shifted to larger  $d$ -spacing compared to the  $\alpha$ -Cr<sub>2</sub>O<sub>3</sub> structure, marked with solid black lines, due to the incorporation of Zr in the  $\alpha$ -Cr<sub>2</sub>O<sub>3</sub>, whereas decrease in lattice spacing above 900 °C, especially for the (104) peak, is attributed to loss of Zr from the initial  $\alpha$ -(Cr,Zr)<sub>2</sub>O<sub>3</sub> structure.

The onset of  $t$ -ZrO<sub>2</sub> formation is visible already around 750 °C for the (101) peak at slightly lower angles compared with the PDF value (PDF-42-1164). An additional diffraction peak is visible at  $\sim 2.55$  Å (110) from around 945 °C, which correlates well with increased intensity for the main  $t$ -ZrO<sub>2</sub> diffraction peak and the shift to smaller lattice spacing for the  $\alpha$ -(Cr,Zr)<sub>2</sub>O<sub>3</sub> structure. At the maximum annealing temperature in air, the  $\alpha$ -(Cr,Zr)<sub>2</sub>O<sub>3</sub> peak intensities are still the

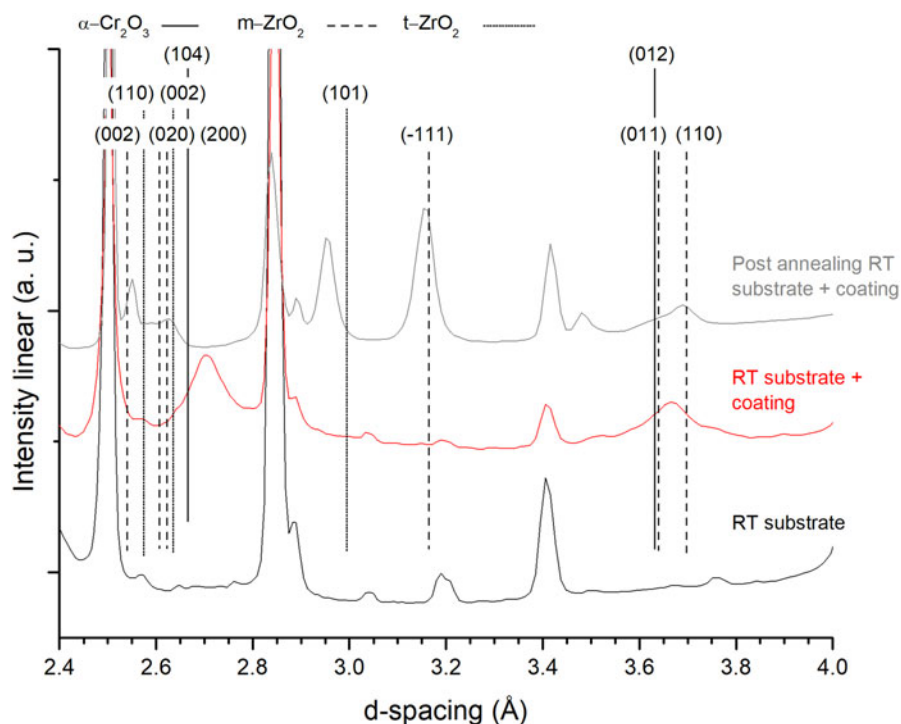


**Figure 2:** X-ray diffractograms of the coating before and after annealing in vacuum up to 1140 °C. Substrate scan at the bottom. Curves shifted for clarity.

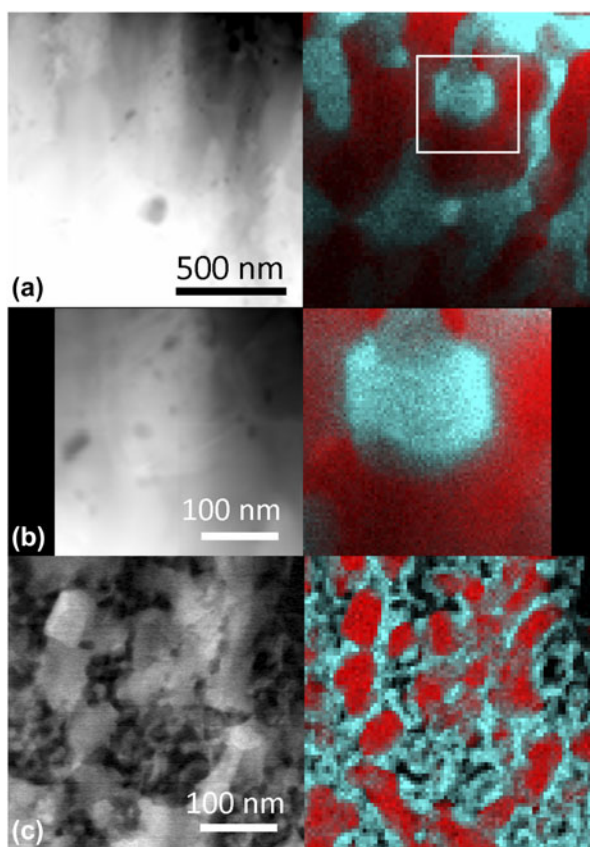


**Figure 3:** (a) Overview STEM micrograph with corresponding EDX map, Zr (turquoise) and Cr (red), of vacuum-annealed sample (up to 1140 °C). (b) Zoom of white box in (a) with the same scale as the work for comparison in (c). (c) Comparison from previous work [43] after isothermal vacuum annealing at 870 °C. The reference sample shows comparable smaller grains, especially for t-ZrO<sub>2</sub>. Observe different sized scale bars. Cross-section samples with growth direction are vertical. (d) Reprinted from L Landälv et al., Structural evolution in reactive RF magnetron sputtered (Cr,Zr)<sub>2</sub>O<sub>3</sub> coatings during annealing, *Acta Materialia* 131, 543-552. Copyright (2017), with permission from Elsevier.

dominant ones over the t-ZrO<sub>2</sub>, contrary to what is seen in the vacuum annealing case.

Figure 5 shows the in situ XRD patterns at RT before and after annealing to 975 °C in air. After annealing, the as-deposited α-(Cr,Zr)<sub>2</sub>O<sub>3</sub> peaks (104) and (012) shifted to match pure α-Cr<sub>2</sub>O<sub>3</sub> phase. The (110) peak is also visible at ~2.48 Å as a shoulder on the substrate peak. The t-ZrO<sub>2</sub> (101) and (110) peaks are present, shifted to slightly smaller *d*-spacing compared with the PDF-card (partly related to different measurement temperatures). The peak at 3.25 Å is attributed to the substrate. Contrary to the vacuum annealing case, no substantial bcc-Cr formation could be observed in XRD. See Supplementary material Figs. S5–S6 for further comparison.

Figure 6(a) shows a TEM EDX map of a sample after air-annealing to 975 °C. The red regions are Cr-rich and the turquoise are Zr-rich. Figure 6(b) shows an EDX map of an isothermally vacuum-annealed sample (810 °C) from Ref. 43

for comparison (same color designation and scale). The microstructure is slightly coarser in the present study, annealed at 165 °C degree higher temperature, but the structural features are still present.

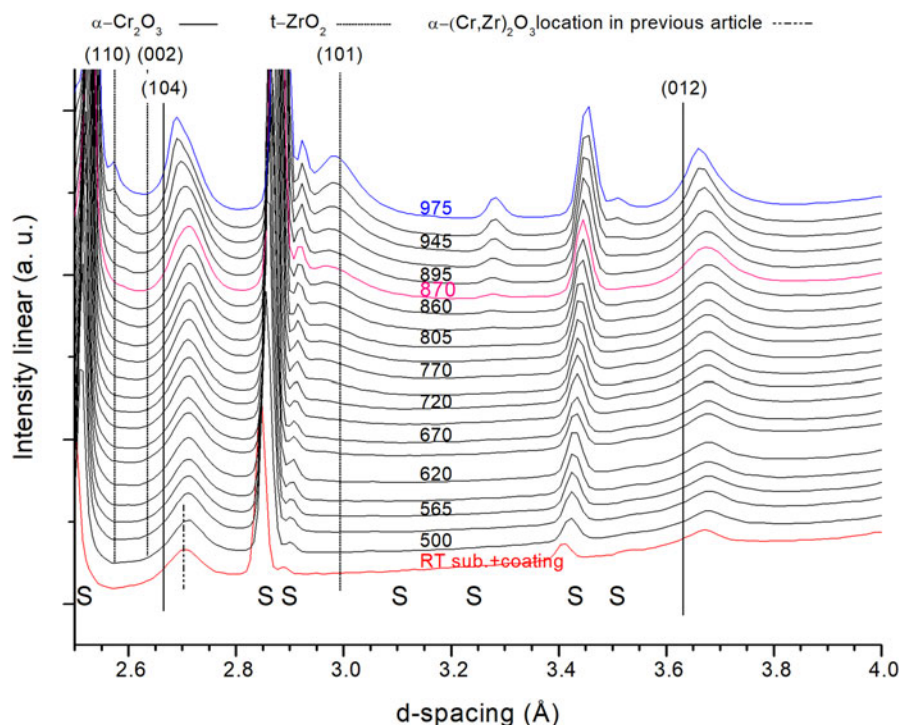
### Top-view SEM on samples before and after annealing in air or vacuum

Figure 7 shows top-view SEM of the (a) as-deposited coating, (b) air-annealed coating, and (c) vacuum-annealed (50 °C/min heating rate) coating. The as-deposited coating shows small feather-like features on the surface. The air-annealed sample (975 °C maximum temperature) shows small grains embedded in a matrix with some larger grains protruding from the surface. The vacuum-annealed sample (1140 °C maximum temperature) shows large voids in between areas with large grains. The grains are ~30/100 nm in size for the air-annealed sample and ~160 nm for the vacuum-annealed sample.

### Discussion

The as-deposited coating was thoroughly characterized in Ref. 43. In summary, the microstructure was shown to consist of elongated, slightly tilted domains in the growth direction. These domains consisted of alternated Zr-rich amorphous oxide and Cr-rich α-(Cr,Zr)<sub>2</sub>O<sub>3</sub> domains, ~3–4 nm in diameter. The alternating phases showed some degree of mutual solid solutions by the smaller Cr<sup>3+</sup> and the larger Zr<sup>4+</sup> ion in the respective structures [41, 44].

Compositional analysis revealed that the as-deposited composition is maintained after annealing to 975 °C in air, whereas the coating annealed in vacuum to 1140 °C indicates loss of Cr as well as slight lower oxygen content, see Table I. XRD in combination with TEM shows monoclinic and tetragonal ZrO<sub>2</sub> and bcc-Cr as final phases in the vacuum-annealed sample. The mix of oxide and metallic phases helps explaining the measured chemical stoichiometry with respect to oxygen in the vacuum-annealed sample. The measured Zr and O contents add up to a ZrO<sub>2</sub>-phase with 0.527 Zr/O ratio, close to the 0.5 stoichiometric ratio for ZrO<sub>2</sub>. Some of the Zr is also most likely present in the Cr phase due to its shift in XRD to 1% larger *d*-spacing. Zr incorporation in bcc-Cr would shift the oxide forming fraction in the coating in the direction of a more stoichiometric ZrO<sub>2</sub>. The shift in Cr/Zr ratio from ~2.8 in the as-deposited film to ~0.5 in the vacuum-annealed coating (50 °C/min) indicates significant loss of Cr from the coating. This motivated additional TEM-EDX measurements on a cross-section sample (not shown). These measurements gave indications of different Cr/Zr ratios depending on the depth in the sample, with Cr/Zr ratio close to the with SEM-EDX determined as deposited ratio when averaging the 1 μm closest to the oxide film–binding layer interface, and a Cr/Zr



**Figure 4:** X-ray diffractograms with increasing annealing temperature of the coating annealed in air up to 975 °C. S = substrate. Blue = maximum temperature achieved when annealing in air and magenta = isothermal vacuum annealing temperature from previous work. Curves shifted for clarity. Temperature is given in °C.

~1 for a compositional average of the top 1 μm of the coating. TEM-EDX averaging the entire coating thickness resulted in Cr/Zr ratios similar to the value obtained for the as-deposited coating with SEM-EDX. The segregation of Cr- and Zr-rich grains on a fairly large length scale (several 100 nm), see Fig. 3, with possible enrichment of Zr-rich grains at the surface, could be the explanation to why top-view SEM-EDX, with limited acquisition depth, shows higher Zr-content than in the as-deposited film. Additional calculations on electron penetration depth and acquisition depth for the generated γ-rays for the top-view SEM-EDX measurement (with 15 keV electrons) showed that the primary information depth was the first ~500 nm, which falls within the high Zr content region identified with TEM-EDX. The absence of a continuous Zr-rich top layer visible with STEM-EDX map on cross-sectional samples made it, however, difficult to assess the coverage and thus the total influence on the SEM-EDX measurements. The loss of Cr through formation of volatile Cr-oxide [45, 46] is judged to be minor due to high vacuum 10<sup>-5</sup> Pa condition for the vacuum-annealed sample in this study.

The top-view SEM-EDX measured 2 at.% Ti in the same vacuum-annealed coating is attributed to possible diffusion of Ti from the substrate within the top ~1.4 μm of the coating (approximately acquisition depth of the SEM probe). A Ti gradient in the film was not possible to corroborate with STEM-TEM due to Ti-TEM grid, causing evenly distributed Ti-signal due to resputtering. The Ti content measured with

SEM-EDX is, however, that low that it is not thought to have influenced the annealing results appreciable.

As calculated in a previous work [43], ZrO<sub>2</sub> is more stable than Cr<sub>2</sub>O<sub>3</sub> under oxygen-deficient conditions due to the lower formation energies of ZrO<sub>2</sub>. ZrO<sub>2</sub> requires more oxygen to form than Cr<sub>2</sub>O<sub>3</sub> and will therefore be able to attract O at the expense of Cr<sub>2</sub>O<sub>3</sub>, leading to the formation of bcc-Cr, which is observed here. The SEM micrographs of the 50 °C/min vacuum-annealed sample also show void formation after annealing to 1140 °C. This is possibly due to the transformation of α-(Cr,Zr)<sub>2</sub>O<sub>3</sub> to bcc-Cr (having higher density) on loss of some oxygen.

The XRD diffractograms of the coating before and after annealing in vacuum to 1140 °C, Fig. 2, show that the main transformation product is a mixture of tetragonal and monoclinic ZrO<sub>2</sub>. The tetragonal phase is probably stabilized by Cr dissolved in the structure, partly explaining the shift to ~1% smaller *d*-spacing. The monoclinic phase, being the RT stable phase for pure ZrO<sub>2</sub>, has been probably formed during cooling of the sample since no such diffraction peaks are clearly observed during heating (Fig. 1). For the monoclinic phase to crystallize exclusively, the trivalent undersized cation concentration (i.e., Cr-content) needs to be below ~1 at.% metal fraction (~2 mol% Cr<sub>2</sub>O<sub>3</sub>) [47, 48] and the grain size larger than ~30 nm [27, 28]. Since the grain size observed in TEM (Fig. 3) is larger than 30 nm,

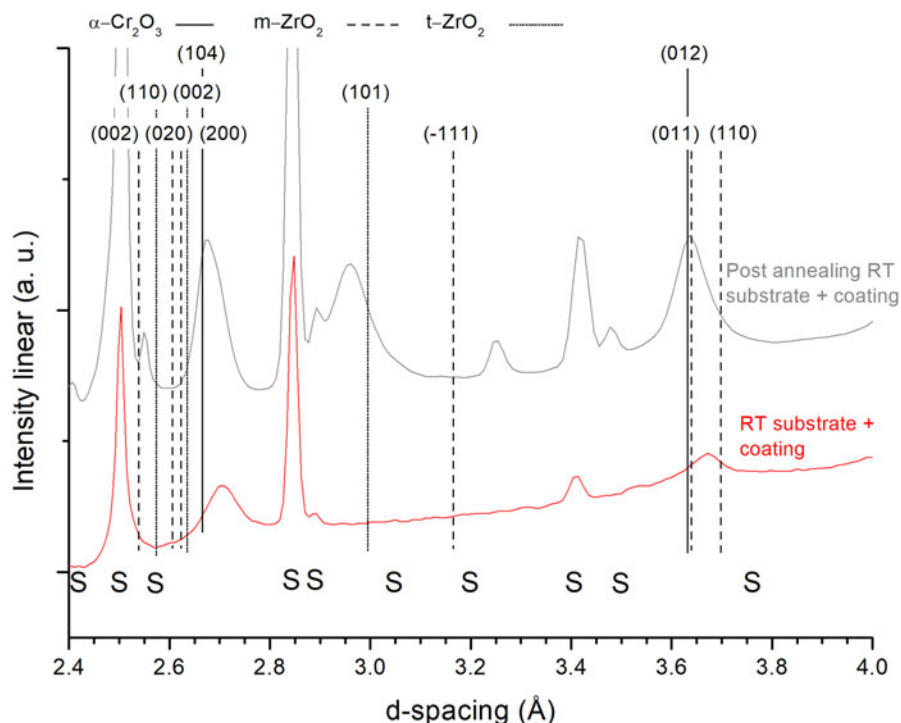


**Figure 5:** X-ray diffractograms of the coating before and after annealing in air up to 975 °C. Curves shifted for clarity. S indicates substrate peaks.

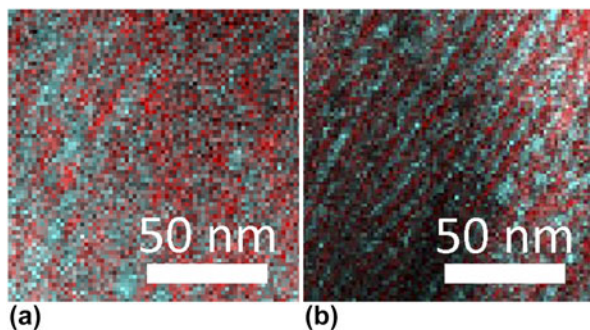


**Figure 6:** TEM-EDX mapping of air- and vacuum-annealed samples. (a) Current work after completing annealing cycle in air to 975 °C. (b) Sample for comparison from previous work [43] after isothermal vacuum annealing at 810 °C, image not previously published. The reference sample shows similar banded microstructure of t-ZrO<sub>2</sub> (turquoise) and α-(CrZr)<sub>2</sub>O<sub>3</sub> (red) but on a finer scale. Cross-section samples with growth direction are vertical.

there must be both ZrO<sub>2</sub> grains with no or very little Cr and some with larger Cr content, stabilizing the tetragonal phase. This is also observed in the different peak shifts for monoclinic and tetragonal phase, small to none for monoclinic (110), (011), and (110) peaks, while significant shift to smaller *d*-spacing for the tetragonal peaks, i.e., (101) and (110), partly explained by the high temperature values from the PDF-card. This mixture of tetragonal and monoclinic phase was not seen in the previous work, where the coating was annealed to a maximum of 870 °C. The difference is

explained by the increased maximum temperature, promoting long-range diffusion and grain growth, which favor the monoclinic phase.

The third phase found in the vacuum-annealed sample is the bcc-Cr. The XRD intensity is too high after annealing to just be attributed to the Cr-containing adhesion layer, partly visible before annealing [bcc Cr-(211) peak]s, Figs. S3–S4. The identification of the phase in the oxide part of the coating in post-annealed sample is done in TEM with a combination of SAED (not shown in the present paper) and TEM-EDX map. The detailed identification of this phase has been shown in previous work [43] and found to be the same in this work. The new in this study, concerning bcc-Cr, is to be able to show the formation onset of bcc-Cr during in situ annealing. The constant X-ray illumination of the adhesion layer zone, since both coating and substrate peaks are visible during the entire annealing study, would result in constant peak intensity for the Cr adhesion layer if no phase transformation occurred. In this study, however, the bcc-Cr (211) peak intensity increases, thus corroborates the formation of more bcc-Cr during high-temperature annealing, starting at ~945 °C, see Fig. S2. This peak increase is closely related to the onset of t-ZrO<sub>2</sub> formation and the disappearance of the α-(Cr,Zr)<sub>2</sub>O<sub>3</sub> phase peaks.

For the air-annealed sample (Fig. 5), the t-ZrO<sub>2</sub> phase is shifted to smaller *d*-spacing after annealing, possibly due to solid solution with the smaller atom Cr, since the macroscopic residual stresses should be annealed out after this high

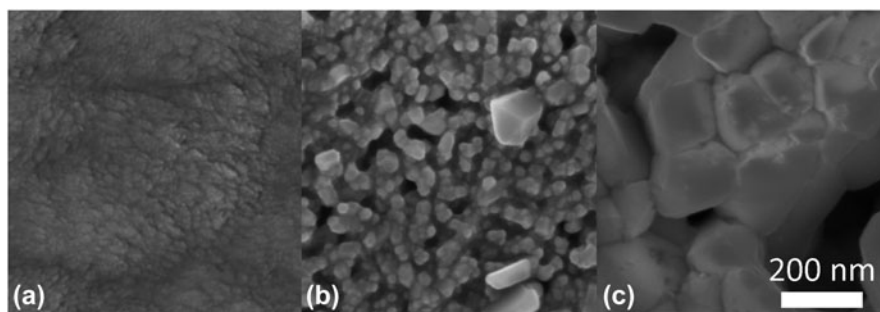


**Figure 7:** SEM micrograph. (a) As-deposited  $(\text{Cr,Zr})_2\text{O}_3$  coating. (b) After annealing in air to 975 °C. (c) After annealing in vacuum to 1140 °C.

annealing temperatures on such a small sample piece. The  $\alpha\text{-Cr}_2\text{O}_3$  phase shows very close match to the PDF-card (PDF-38-1479), only slightly larger  $d$ -spacing, which could indicate some residual Zr in the lattice. No monoclinic  $\text{ZrO}_2$  or bcc-Cr is visible in the air-annealed sample with XRD (Fig. 5). The TEM-EDX map confirms a similar segregation pattern (Fig. 6), as was observed in previous vacuum annealing work, where alternating  $\alpha\text{-Cr}_2\text{O}_3$  and  $t\text{-ZrO}_2$  regions were determined. Altogether, the same conclusion about the phases can be drawn for this air-annealed sample.

Since the maximum annealing temperature for the air- and vacuum-annealed samples ended up not being the same, other comparisons than the direct comparison of the post-annealed samples need to be performed. The temperature control was also different between the two setups, making the heating rate in the air-annealed sample closer to 10 °C/min, in steps of 5 min plateaus. Thus, when comparing the 50 °C/min vacuum annealing with the slower heating rate air sample, the changes in the air sample would be closer to equilibrium at a given temperature of comparison. Comparison of the XRD of the air-annealed and vacuum-annealed samples at the maximum temperature of the air-annealed sample allow for the most one-to-one like comparison of the effect of annealing atmosphere possible in this setup. The integrated peak intensity ratio between the (101)  $t\text{-ZrO}_2$  and the  $\alpha\text{-Cr}_2\text{O}_3$  peaks, (104) and (012), at this temperature differs significantly between the samples annealed in vacuum and the one in air at that temperature (Supplementary material, Fig. S7). For the vacuum-annealed sample, the ratios are 3.6 and 5.1 [(101)/(104) and (101)/(012)], while for the air-annealed sample, the ratios are 1.3 and 2.9. The air-annealed sample shows higher or comparable intensity for the  $\alpha\text{-Cr}_2\text{O}_3$  peaks, shown as a lower ratio value, compared with the  $t\text{-ZrO}_2$  peak at this temperature. This indicates higher stability of this  $(\text{Cr,Zr})_2\text{O}_3$  coating in air than under vacuum conditions. The absence of high-intensity Cr (211) peak at 1.19 Å (Supplementary material, Fig. S8) help explain why the  $t\text{-ZrO}_2$  phase show lower diffraction intensity. This is probably due to its hindered formation/grain growth by the in air more stable  $\alpha\text{-Cr}_2\text{O}_3$  phase which is not being

transformed to bcc-Cr. The 1.19 Å peak at 975 °C in Fig. S8 is attributed to the (211) peak of a bcc-Cr phase with some dissolved Zr, resulting in the ~1% increase in lattice spacing. The solubility of Zr in Cr is according to the phase diagram limited to ~0.6 at.% under thermodynamic equilibrium [49]. There is also a (213)  $t\text{-ZrO}_2$  peak position in the same  $d$ -spacing range if compared with lower order peak position at this temperature. The observed intensity for the 1.19 Å peak is, however, large compared with the (211) and (103)  $t\text{-ZrO}_2$  peaks at 1.54 and 1.57 Å. The two later should have significantly higher intensities than the (213)  $t\text{-ZrO}_2$  peak according to the PDF-card. Even considering texture effects, this is likely a significant difference. Texture effects should as well be intrinsically reduced by the way the diffractogram intensities are summed over 180° azimuth angle, covering a large part of the reciprocal space. An additional annealing run was performed in vacuum, with lower heating rate (10 °C/min), which is more explained in Supplementary material and shown in Figs. S7–S9. The higher  $t\text{-ZrO}_2/\alpha\text{-Cr}_2\text{O}_3$  peak ratio for the slowly vacuum-annealed sample indicates the higher degree of conversion to  $t\text{-ZrO}_2$  when the heating rate is slower (more similar to the air-annealed sample).

The difference in max annealing temperature and slightly different heating rate, where the maximum temperature is judged to be the more important parameter, limit the possibility of claiming better thermal stability of the air-annealed sample above 975 °C. However, the above-explained difference in peak ratios and the existence of bcc-Cr in the vacuum-annealed samples already at this temperature give a strong indication that the coating is more stable in air than in vacuum.

The hardness of the air-annealed sample remained close to the as-deposited value of 19.6 GPa after the annealing to 975 °C. Thus, the as-deposited hardness level may be retained after annealing to higher temperatures than in Ref. 43, if done in air and for limited time (here, ~45 min with temperature higher than 810 °C). The retained hardness after the annealing can be explained by the crystallization of  $t\text{-ZrO}_2$ , the limited grain growth, and retained microstructure, the last two being observed in the STEM-EDX map [Fig. 6(a)]. This can also be



compared to an 810 °C isothermally vacuum-annealed coating [Fig. 6(b)], which is a sample from Ref. 43. The vacuum-annealed sample in this study shows a hardness, i.e., lower than that of the as-deposited sample, more corresponding to values of m-ZrO<sub>2</sub>, ~10 GPa [50], not even considering the negative effect of voids on the hardness, as observed in Fig. 7. The spread in hardness values was smaller for the vacuum-annealed sample than in the air-annealed case, even considering the voids. This is possibly due to the metallic Cr fraction in the vacuum-annealed coating, resulting in a slight increase in deformability. The hardness of nc-Cr [51], highly dependent on grain size, is also in the range of the hardness of the vacuum-annealed sample measured in this study.

## Conclusions

We have studied the behavior of Cr-rich  $\alpha$ -(Cr,Zr)<sub>2</sub>O<sub>3</sub> solid solution coatings on annealing in vacuum and in air atmosphere with in situ synchrotron XRD as well as post-annealing TEM, SEM, and hardness measurements with nanoindentation.

The annealing in vacuum shows t-ZrO<sub>2</sub> formation starting ~800 °C, which is followed by decomposition of the  $\alpha$ -Cr<sub>2</sub>O<sub>3</sub> structure in conjunction with bcc-Cr formation, starting at ~950 °C. The resulting coating after annealing to 1140 °C is a coarse grained mixture of t-ZrO<sub>2</sub>, m-ZrO<sub>2</sub>, and bcc-Cr, with intermediate voids.

The air-annealed sample shows t-ZrO<sub>2</sub> formation starting at ~750 °C. The  $\alpha$ -(Cr,Zr)<sub>2</sub>O<sub>3</sub> starts to transform to  $\alpha$ -Cr<sub>2</sub>O<sub>3</sub> at ~945 °C at the same time as the t-ZrO<sub>2</sub> formation increases. The resulting coating after annealing to 975 °C is a mixture of  $\alpha$ -Cr<sub>2</sub>O<sub>3</sub> with dissolved Zr and t-ZrO<sub>2</sub> with dissolved Cr. The microstructure coarsened slightly, but the mechanical properties are maintained, with no detectable bcc-Cr formation.

Comparing the relative integrated peak intensities of t-ZrO<sub>2</sub> and  $\alpha$ -Cr<sub>2</sub>O<sub>3</sub> at 975 °C, a larger t-ZrO<sub>2</sub> fraction is shown in the vacuum-annealed coating, compared with the air-annealed coating, already at this temperature. The results indicate that the studied pseudo-binary oxide is more stable in air atmosphere than in vacuum. Using relevant annealing atmosphere should be considered to ensure an optimization to wear-resistant coating applications in future studies.

## Experimental details

The deposition of the Cr–Zr–O coatings was performed with stationary substrate (TiAl alloy) in a Leybold Z 550 RF magnetron sputtering deposition equipment with the base pressure of the chamber being  $6 \times 10^{-4}$  Pa. An ~250 nm Cr adhesive layer was deposited in DC mode in a separate process, while both ~250 nm CrZr and 4.5  $\mu$ m CrZrO depositions were done in the RF mode with a segmented Cr/Zr-target at 500 °C. Full description is found in previous work [43].

The substrate used for deposition was a TiAl alloy, commercial name TNB-V2, with a composition of 47 at.% Ti, 45 at.% Al, and 8 at.% Nb. This alloy was used for the annealing experiment since it is known to resist high temperatures up to 900 °C with maintained mechanical properties. The samples for the X-ray synchrotron radiation annealing test were cut into ~2 mm thick pieces (perpendicular to the sample surface) from the same deposited half disc used/described in previous study [43].

The chemical composition of the as-deposited coating, prior to the annealing experiment, was determined by EPMA (Camebax Microbeam), as reported in Ref. 43. The annealed coating and an as-deposited sample piece from the same original larger sample was imaged in top view with an SEM, Leo 1550 Gemini field emission gun, with 5 kV acceleration voltage and in-lens detector. The chemical composition was determined with an 80 mm<sup>2</sup> X-Max Oxford Instruments EDX equipment installed on the same SEM system, using 15 keV acceleration voltage. At this accelerating voltage, the penetration depth of the beam is not sufficient to reach the substrate. Carbon detected with EDX was not considered since previous EPMA measurements showed below 1 at.% C, N, and Ar in the as-deposited sample. The previous EPMA measurement of the as-deposited coating served as a reference for the EDX measurements and matched well.

In situ wide-angle X-ray scattering was performed in transmission mode at the High Energy Materials Science Beamline P07 at Petra III, DESY Hamburg, using a 5  $\mu$ m high and 20  $\mu$ m wide X-ray beam with an energy of 78 keV (wavelength 0.159 Å). The diffracted X-rays were collected on a PerkinElmer 2D detector 2048  $\times$  2048 pixels (41  $\times$  41 cm size), which was positioned ~1.4 m after the sample. For both the air and vacuum annealing experiments, the diffractograms were recorded continuously in a process that took ~13 s in total (5 exposures of 1 s, each including equally long background exposures), hence ~4 diffractograms/min. The data were evaluated by converting the 2D-diffractogram to 1D diffractograms by integrating the data in the upper half of the detector. The 2D data from the bottom half of the detector were omitted due to the higher absorption of X-rays transmitted through the substrate and sample holder.

The annealing was performed using two different setups, both in transmission geometry, one for air annealing and other for vacuum annealing.

The air annealing setup consisted of a suspended quartz rod, on which the sample rested on (open air, atmospheric pressure, convective induced air flow). The sample was heated from above with a focused Osram Xenophot halogen lamp (MR16 64635 HLX). The temperature was set by the voltage applied to the heating lamp. Prior to the test, an approximate calibration of the temperature was done using a thermocouple

type K at the sample position. The exact sample temperature was later calculated through the thermal expansion of the substrate (see below). The annealing test started by heating the sample to approximately the deposition temperature, followed by an 11 min hold period before the gradual heating started. The voltage was then increased in steps of 0.5 V every 5 min to a maximum of 17.5 V, corresponding to a total of 110 min before cooling started. Cooling back to RT took 21 min. Diffractograms were acquired before and after the annealing and continuously during annealing according to the previously specified procedure. The diffractograms shown from the coating annealed in air were selected to be from the end of each 5 min hold period.

The vacuum annealing was performed in an ultra-high vacuum deposition system (base pressure was  $\sim 3 \times 10^{-5}$  Pa, not baked) with the possibility to investigate the sample in situ with XRD while heating the sample. The deposition system is described in detail elsewhere [52]. The heating was carried out with an infrared laser directed on the backside of a SiC sample holder plate, on which the sample rested on without any clamp or thermal conduction paste. The temperature was controlled by a pyrometer reading taken from the same side as the laser heating. The temperature on the sample surface was calibrated to the temperature readout from the pyrometer by a K-type thermocouple mounted on top of a sapphire substrate prior to the annealing test. The sample temperature as determined by the thermocouple in the vacuum setup was considered to be the most accurate temperature measurement and is the temperature referred to in the remaining part of the article. The heating rate during annealing in vacuum was 50 °C/min from the starting hold temperature of 400 °C. The annealing time from this hold temperature until the maximum temperature of 1140 °C was 21.5 min, followed by a hold period of 7 min. The time to reach the same temperature as the maximum temperature reached for the air-annealed sample was 15.5 min, and the discrepancy in maximum annealing temperature is treated in the next paragraph.

Since the uncertainty of sample temperature was larger for the air-annealing setup, the temperature of the air-annealed sample was obtained by determining the peak position of three substrate peaks ( $d$ -spacing 1.17, 2.20, and 4.06 Å) and comparing that with the substrate peak positions of the vacuum-annealed sample. By assuming the same thermal expansion coefficient for the air-annealed sample and the vacuum-annealed sample, an equivalent sample temperature was determined for the air-annealed sample. Further description about this procedure can be found in the Supplementary material, summarized in Fig. S1 (substrate  $d$ -spacing as a function of vacuum calibrated  $T$  for air- and vacuum-annealed samples). This recalibration showed that the maximum temperature reached for the air-annealed samples was 975 °C,  $\sim 165$  °C lower than the maximum achieved temperature (1140 °C) for the vacuum-annealed sample. This

difference in maximum attained annealing temperature needs to be considered when comparing the post-annealed properties. The diffractograms shown from the vacuum-annealed sample were selected in a way such that the sample had the same temperature as the ones selected from the air-annealed sample.

Overview STEM micrographs were acquired with an FEI Tecnai G2 TF20 UT TEM, using high-angle annular dark field mode, equipped with a field emission gun operated at a voltage of 200 kV and an EDX from EDAX with an energy resolution of 130 eV.

The hardness was measured with a UMIS2000 nanoindentation system equipped with a Berkovich indenter. 49 quasi static (closed loop) indents were made on the as-deposited and as-annealed surfaces with a maximum load of 30 mN (maximum depth  $\sim 340$  nm for the softest sample, being well below 10% of total coating thickness). The data were analyzed by the technique of Oliver and Pharr [53] and reported here are the mean value and the standard deviation from 46 (as-deposited), 44 (vacuum annealed 50 °C/min), and 30 (air-annealed) indents with valid loading curves, respectively. The machine compliance was calibrated to 0.2 nm/mN.

## Acknowledgments

The Swedish Research Council (VR, Grant No. 621-2012-4368) is acknowledged for financial support for L.L.'s industry Ph.D. studies with AB Sandvik Coromant. P.E. acknowledges the Knut and Alice Wallenberg Foundation through a Fellowship grant, and P.E. and J.B. acknowledge the Swedish Government Strategic Research Area in Materials Science on Functional Materials at Linköping University (Faculty Grant SFO-Mat-LiU No. 2009 00971). B.A. acknowledges financial support from the Swedish Research Council (VR) through the International Career Grant No. 330-2014-6336 and by Marie Skłodowska Curie Actions, Cofund, Project INCA 600398, as well as from the Swedish Foundation for Strategic Research (SSF) through the Future Research Leaders 6 program. We acknowledge financial support from the Swedish Research Council via the Röntgen Ångström Cluster (RÅC) Frame Program (No. 2011–6505) and the German Federal Ministry of Education and Research (BMBF) under Grant No. 05K12CG1.

## Supplementary material

To view supplementary material for this article, please visit <https://doi.org/10.1557/jmr.2019.340>.

## References

1. **D.T. Quinto:** Mechanical property and structure relationships in hard coatings for cutting tools. *J. Vac. Sci. Technol., A* **6**, 2149 (1988).

2. **A. Khatibi, A. Genvad, E. Göthelid, J. Jensen, P. Eklund, and L. Hultman:** Structural and mechanical properties of corundum and cubic  $(Al_xCr_{1-x})_{2+y}O_{3-y}$  coatings grown by reactive cathodic arc evaporation in as-deposited and annealed states. *Acta Mater.* **61**, 4811 (2013).
3. **J. Ramm, M. Ante, T. Bachmann, B. Widrig, H. Brändle, and M. Döbeli:** Pulse enhanced electron emission (P3e™) arc evaporation and the synthesis of wear resistant Al–Cr–O coatings in corundum structure. *Surf. Coat. Technol.* **202**, 876 (2007).
4. **P. Eklund, M. Sridharan, M. Sillassen, and J. Böttiger:**  $\alpha$ -Cr<sub>2</sub>O<sub>3</sub> template-texture effect on  $\alpha$ -Al<sub>2</sub>O<sub>3</sub> thin-film growth. *Thin Solid Films* **516**, 7447 (2008).
5. **P. Hones, F. Levy, and N.X. Randall:** Influence of deposition parameters on mechanical properties of sputter-deposited Cr<sub>2</sub>O<sub>3</sub> thin films. *J. Mater. Res.* **14**, 3623 (1999).
6. **P. Jin, G. Xu, M. Tazawa, K. Yoshimura, D. Music, J. Alami, and U. Helmersson:** Low temperature deposition of  $\alpha$ -Al<sub>2</sub>O<sub>3</sub> thin films by sputtering using a Cr<sub>2</sub>O<sub>3</sub> template. *J. Vac. Sci. Technol., A* **20**, 2134 (2002).
7. **J.M. Andersson, Z. Czigany, P. Jin, and U. Helmersson:** Microstructure of  $\alpha$ -alumina thin films deposited at low temperatures on chromia template layers. *J. Vac. Sci. Technol., A* **22**, 117 (2004).
8. **D.E. Ashenford, F. Long, W.E. Hagston, B. Lunn, and A. Matthews:** Experimental and theoretical studies of the low-temperature growth of chromia and alumina. *Surf. Coat. Technol.* **116**, 699 (1999).
9. **M. Witthaut, R. Cremer, K. Reichert, and D. Neuschütz:** Preparation of Cr<sub>2</sub>O<sub>3</sub>–Al<sub>2</sub>O<sub>3</sub> solid solutions by reactive magnetron sputtering. *Mikrochim. Acta.* **133**, 191 (2000).
10. **J. Ramm, M. Ante, H. Brandle, A. Neels, A. Dommann, and M. Döbeli:** Thermal stability of thin film corundum-type solid solutions of  $(Al_{1-x}Cr_x)_2O_3$  synthesized under low-temperature non-equilibrium conditions. *Adv. Eng. Mater.* **9**, 604 (2007).
11. **K. Pedersen, J. Böttiger, M. Sridharan, M. Sillassen, and P. Eklund:** Texture and microstructure of Cr<sub>2</sub>O<sub>3</sub> and (Cr,Al)<sub>2</sub>O<sub>3</sub> thin films deposited by reactive inductively coupled plasma magnetron sputtering. *Thin Solid Films* **518**, 4294 (2010).
12. **L. de Abreu Vieira, M. Döbeli, A. Dommann, E. Kalchbrenner, A. Neels, J. Ramm, H. Rudigier, J. Thomas, and B. Widrig:** Approaches to influence the microstructure and the properties of Al–Cr–O layers synthesized by cathodic arc evaporation. *Surf. Coat. Technol.* **204**, 1722 (2010).
13. **M. Pohler, R. Franz, J. Ramm, P. Polcik, and C. Mitterer:** Cathodic arc deposition of (Al,Cr)<sub>2</sub>O<sub>3</sub>: Macroparticles and cathode surface modifications. *Surf. Coat. Technol.* **206**, 1454 (2011).
14. **D. Diechle, M. Stueber, H. Leiste, S. Ulrich, and V. Schier:** Combinatorial approach to the growth of  $\alpha$ -(Al<sub>1-x</sub>Cr<sub>x</sub>)<sub>2</sub>O<sub>3</sub> solid solution strengthened thin films by reactive r.f. magnetron sputtering. *Surf. Coat. Technol.* **204**, 3258 (2010).
15. **A. Khatibi, J. Palisaitis, C. Höglund, A. Eriksson, P.O.Å. Persson, J. Jensen, J. Birch, P. Eklund, and L. Hultman:** Face-centered cubic  $(Al_{1-x}Cr_x)_2O_3$ . *Thin Solid Films* **519**, 2426 (2011).
16. **H. Najafi, A. Karimi, P. Dessarzin, and M. Morstein:** Formation of cubic structured  $(Al_{1-x}Cr_x)_{2+\delta}O_3$  and its dynamic transition to corundum phase during cathodic arc evaporation. *Surf. Coat. Technol.* **214**, 46 (2013).
17. **J.A. Krogstad, M. Lepple, Y. Gao, D.M. Lipkin, and C.G. Levi:** Effect of yttria content on the zirconia unit cell parameters. *J. Am. Ceram. Soc.* **94**, 4548 (2011).
18. **O. Fabrichnaya, C. Wang, M. Zinkevich, C.G. Levi, and F. Aldinger:** Phase equilibria and thermodynamic properties of the ZrO<sub>2</sub>–GdO<sub>1.5</sub>–YO<sub>1.5</sub> system. *J. Phase Equilib. Diffus.* **26**, 591 (2005).
19. **D. Simeone, G. Baldinozzi, D. Gosset, M. Dutheil, A. Bulou, and T. Hansen:** Monoclinic to tetragonal semireconstructive phase transition of zirconia. *Phys. Rev. B* **67**, 064111 (2003).
20. **J. Swab:** *Role of Oxide Additives in Stabilizing Zirconia for Coating Applications*; Army Research Laboratory (ARL), Aberdeen Proving Ground, Maryland. Report number ARL-TR-2591, 2001.
21. **I. Nettleship and R. Stevens:** Tetragonal zirconia polycrystal (TZP)—A review. *Int. J. High Technol. Ceram.* **3**, 1 (1987).
22. **A. Feuerstein, J. Knapp, T. Taylor, A. Ashary, A. Bolcavage, and N. Hitchman:** Technical and economical aspects of current thermal barrier coating systems for gas turbine engines by thermal spray and EB-PVD: A review. *J. Therm. Spray Technol.* **17**, 199 (2008).
23. **Y. Wang and C. Zhou:** Microstructure and thermal properties of nanostructured gadolinia doped yttria-stabilized zirconia thermal barrier coatings produced by air plasma spraying. *Ceram. Int.* **42**, 13047 (2016).
24. **R. Vassen, A. Stuke, and D. Stover:** Recent developments in the field of thermal barrier coatings. *J. Therm. Spray Technol.* **18**, 181 (2009).
25. **C. Mercer, J.R. Williams, D.R. Clarke, and A.G. Evans:** On a ferroelastic mechanism governing the toughness of metastable tetragonal-prime (t') yttria-stabilized zirconia. *Proc. R. Soc., Ser. A* **463**, 1393 (2007).
26. **G. Soon, B. Pingguan-Murphy, K.W. Lai, and S.A. Akbar:** Review of zirconia-based bioceramic: Surface modification and cellular response. *Ceram. Int.* **42**, 12543 (2016).
27. **G. Baldinozzi, D. Simeone, D. Gosset, and M. Dutheil:** Neutron diffraction study of the size-induced tetragonal to monoclinic phase transition in zirconia nanocrystals. *Phys. Rev. Lett.* **90**, 216103 (2003).
28. **R.C. Garvie:** The occurrence of metastable tetragonal zirconia as a crystallite size effect. *J. Phys. Chem.* **69**, 1238 (1965).
29. **S.D. Park, J.M. Vohs, and R.J. Gorte:** Direct oxidation of hydrocarbons in a solid-oxide fuel cell. *Nature* **404**, 265 (2000).
30. **N.Q. Minh:** Solid oxide fuel cell technology? Features and applications. *Solid State Ionics* **174**, 271 (2004).

31. N.Q. Minh and M.B. Mogensen: Reversible solid oxide fuel cell technology for green fuel and power production. *Electrochem. Soc. Interface* **22**, 55 (2013).
32. S. Sonderby, A.J. Nielsen, B.H. Christensen, K.P. Almqvist, J. Lu, J. Jensen, L.P. Nielsen, and P. Eklund: Reactive magnetron sputtering of uniform yttria-stabilized zirconia coatings in an industrial setup. *Surf. Coat. Technol.* **206**, 4126 (2012).
33. S. Sonderby, B.H. Christensen, K.P. Almqvist, L.P. Nielsen, and P. Eklund: Industrial-scale high power impulse magnetron sputtering of yttria-stabilized zirconia on porous NiO/YSZ fuel cell anodes. *Surf. Coat. Technol.* **281**, 150 (2015).
34. S.H. Song, J. Moon, J.H. Kim, J. Hong, J-H. Lee, H-W. Lee, B-K. Kim, and H. Kim: Panoramic alloying of cobalt in CeO<sub>2</sub>-ZrO<sub>2</sub> solid solutions for superior oxygen-storage capacity. *Acta Mater.* **113**, 206 (2016).
35. C. Descorme, Y. Madier, and D. Duprez: Infrared study of oxygen adsorption and activation on cerium-zirconium mixed oxides. *J. Catal.* **196**, 167 (2000).
36. S. Hirano, M. Yoshinaka, K. Hirota, and O. Yamaguchi: Formation, characterization, and hot isostatic pressing of Cr<sub>2</sub>O<sub>3</sub>-doped ZrO<sub>2</sub> (0, 3 mol% Y<sub>2</sub>O<sub>3</sub>) prepared by hydrazine method. *J. Am. Ceram. Soc.* **79**, 171 (1996).
37. S. Ram: Synthesis and structural and optical properties of metastable ZrO<sub>2</sub> nanoparticles with intergranular Cr<sup>3+</sup>/Cr<sup>4+</sup> doping and grain surface modification. *J. Mater. Sci.* **38**, 643 (2003).
38. G. Stefanic, S. Popovic, and S. Music: Influence of Cr<sub>2</sub>O<sub>3</sub> on the stability of low temperature t-ZrO<sub>2</sub>. *Mater. Lett.* **36**, 240 (1998).
39. Y. Takano, T. Komeda, M. Yoshinaka, K. Hirota, and O. Yamaguchi: Fabrication, microstructure, and mechanical properties of Cr<sub>2</sub>O<sub>3</sub>/ZrO<sub>2</sub>(2.5Y) composite ceramics in the Cr<sub>2</sub>O<sub>3</sub>-rich region. *J. Am. Ceram. Soc.* **81**, 2497 (1998).
40. S. Spitz, M. Stueber, H. Leiste, S. Ulrich, and H.J. Seifert: Microstructure evolution of radio-frequency magnetron sputtered oxide thin films in the Cr-Zr-O system. *Thin Solid Films* **548**, 143 (2013).
41. R. Shannon: Revised effective ionic radii and systematic studies of interatomic distances in halides and chalcogenides. *Acta Crystallogr. A* **32**, 751 (1976).
42. D. Rafaja, C. Wüstefeld, G. Abrasonis, S. Braeunig, C. Baetzhtz, F. Hanzig, M. Dopita, M. Krause, and S. Gemming: Thermally induced formation of metastable nanocomposites in amorphous Cr-Zr-O thin films deposited using reactive ion beam sputtering. *Thin Solid Films* **612**, 430 (2016).
43. L. Landälv, J. Lu, S. Spitz, H. Leiste, S. Ulrich, M.P. Johansson-Jöesaar, M. Ahlgren, E. Göthelid, B. Alling, L. Hultman, M. Stüber, and P. Eklund: Structural evolution in reactive RF magnetron sputtered (Cr,Zr)<sub>2</sub>O<sub>3</sub> coatings during annealing. *Acta Mater.* **131**, 543 (2017).
44. R.D. Shannon and C.T. Prewitt: Effective ionic radii in oxides and fluorides. *Acta Crystallogr. A* **25**, 925 (1969).
45. H.C. Graham and H.H. Davis: Oxidation/vaporization kinetics of Cr<sub>2</sub>O<sub>3</sub>. *J. Am. Ceram. Soc.* **54**, 89 (1971).
46. H. Hindam and D.P. Whittle: Microstructure, adhesion and growth kinetics of protective scales on metals and alloys. *Oxid. Met.* **18**, 245 (1982).
47. P. Li, I-W. Chen, and J.E. Penner-Hahn: Effect of dopants on zirconia stabilization—An X-ray absorption study: I, trivalent dopants. *J. Am. Ceram. Soc.* **77**, 118 (1994).
48. M. Yoshimura, M. Yashima, T. Noma, and S. Sömiya: Formation of diffusionlessly transformed tetragonal phases by rapid quenching of melts in ZrO<sub>2</sub>-RO<sub>1.5</sub> systems (R = rare earths). *J. Mater. Sci.* **25**, 2011 (1990).
49. B. Predel: *Cr-Zr (Chromium-Zirconium)* (Springer, Berlin, Heidelberg, 1994); p. 1.
50. S.A. Catledge, M. Cook, Y.K. Vohra, E.M. Santos, M.D. McClenny, and K. David Moore: Surface crystalline phases and nanoindentation hardness of explanted zirconia femoral heads. *J. Mater. Sci.: Mater. Med.* **14**, 863 (2003).
51. D. Wu, J. Zhang, J.C. Huang, H. Bei, and T.G. Nieh: Grain-boundary strengthening in nanocrystalline chromium and the Hall-Petch coefficient of body-centered cubic metals. *Scr. Mater.* **68**, 118 (2013).
52. J.L. Schroeder, W. Thomson, B. Howard, N. Schell, L-Å. Näslund, L. Rogström, M.P. Johansson-Jöesaar, N. Ghafoor, M. Odén, E. Nothnagel, A. Shepard, J. Greer, and J. Birch: Industry-relevant magnetron sputtering and cathodic arc ultra-high vacuum deposition system for in situ X-ray diffraction studies of thin film growth using high energy synchrotron radiation. *Rev. Sci. Instrum.* **86**, 095113 (2015).
53. W.C. Oliver and G.M. Pharr: An improved technique for determining hardness and elastic modulus using load and displacement sensing indentation experiments. *J. Mater. Res.* **7**, 1564 (1992).